

Radio Pulse Profile Evolution of Magnetar Swift J1818.0–1607

R. Fisher,^{1*} E. M. Butterworth,¹ K. M. Rajwade,² B. W. Stappers,¹ G. Desvignes,³ R. Karuppusamy,³ M. Kramer,³ K. Liu,³ A. G. Lyne,¹ M. B. Mickaliger,¹ B. Shaw,¹ and P. Weltevrede¹

¹Jodrell Bank Centre for Astrophysics, University of Manchester, Oxford Road, Manchester M13 9PL, UK

²ASTRON, the Netherlands Institute for Radio Astronomy, Oude Hoogeveensedijk 4, NL-7991 PD Dwingeloo, the Netherlands

³Max-Planck-Institut für Radioastronomie, Auf dem Hügel 69, D-53121 Bonn, Germany

Accepted XXX. Received YYY; in original form ZZZ

ABSTRACT

The shape and polarisation properties of the radio pulse profiles of radio-loud magnetars provide a unique opportunity to investigate their magnetospheric properties. Gaussian Process Regression analysis was used to investigate the variation in the total intensity shape of the radio pulse profiles of the magnetar Swift J1818.0–1607. The observed profile shape was found to evolve through three modes between MJDs 59104 and 59365. The times at which these transitions occurred coincided with changes in the amplitude of modulations in the spin-down rate. The amount of linear and circular polarisation was also found to vary significantly with time. Lomb-Scargle periodogram analysis of the spin-down rate revealed three possibly harmonically related frequencies. This could point to the magnetar experiencing seismic activity. However, no profile features exhibited significant periodicity, suggesting no simple correlations between the profile variability and fluctuations of the spin-down on shorter timescales within the modes. Overall, this implies the mode changes seen are a result of local magnetospheric changes, with other theories, such as precession, less able to explain these observations.

Key words: stars: neutron – stars: magnetars – pulsars: individual: PSR J1818–1607.

1 INTRODUCTION

Magnetars are a subclass of neutron stars that are characterised by large inferred magnetic fields (10^{14} – 10^{15} G), rotation periods of 1–12 s, and characteristic ages less than 200,000 years (Kaspi & Beloborodov 2017; Lyne et al. 2022). Magnetars are observed to produce high-energy emission in the form of bursts and persistent X-ray and γ -ray emission that is thought to be powered by their magnetic fields. This is in contrast to radio pulsars, which are powered by their rotational energy. Six magnetars have been seen to emit pulses of radio emission, which are much more variable in time than those of standard radio pulsars in terms of flux density, profile shape, and polarisation (e.g. Kramer et al. 2007; Camilo et al. 2007c; Levin et al. 2010; Keith et al. 2011; Lee et al. 2013; Shannon & Johnston 2013; Lower et al. 2020; Kirsten et al. 2021). These emission characteristics are also shared with high magnetic field strength pulsars that occasionally display magnetar-like outbursts (e.g., PSR J1119–6127, Dai et al. (2018)). The onset of radio emission in these objects typically occurs after high-energy outbursts (Kaspi & Beloborodov 2017) and may therefore be associated with the twisting of the magnetosphere. The radio emission is thought to originate from the “j-bundle” of field lines (Beloborodov 2009).

The magnetar Swift J1818.0–1607 was discovered in March 2020 via its X-ray outburst (Stamatikos et al. 2020) and further observations detected pulsed radio emission (Karuppusamy et al. 2020; Rajwade et al. 2020) making it only the fifth radio-loud magnetar (Lower et al. 2020). The magnetar has a rotation period of 1.36 s (Hu

et al. 2020b) and therefore has the fastest rotation rate of any magnetar discovered to date. Previous work on the radio pulse profiles of the magnetar (Champion et al. 2020; Lower et al. 2020, 2021; Rajwade et al. 2022) has shown a high variability in their shape and polarisation properties, suggesting it has a very dynamic magnetosphere. The radio emission was found to be between 80–100 percent linearly polarised and to exhibit a mode change by Lower et al. (2020) and Champion et al. (2020). This is similar to findings for other magnetars. However, features such as its radio spectrum being unusually steep early on in its outburst before later flattening to values more typical of magnetars (Lower et al. 2020; Champion et al. 2020) suggest this object may provide a crucial link between the high-magnetic-field radio pulsar and magnetar populations (Hu et al. 2020a). The magnetar 1E 1547.0–5408 has also been shown to display pulse profile variability that differs from that of normal pulsars, as well as a high percentage of linear polarisation, although this was seen to drop significantly at lower frequencies (Camilo et al. 2007c). The radio pulse profiles of magnetars XTE J1810–197 (Kramer et al. 2007; Camilo et al. 2007a,b) and PSR J1622–4950 (Levin et al. 2012) also have very high levels of linear polarisation, with dramatic variations in shape and polarisation fraction. In the latter, the linear polarisation fraction showed signs of decreasing at lower observing frequencies (Levin et al. 2010, 2012). Similar behaviour has also been observed in 1E 1547.0–5408 (Camilo et al. 2008). Investigating the unusual polarisation characteristics of magnetars is therefore important, as it will provide insight into the radio emission mechanism, magnetospheric properties, and magnetic field geometry of these objects.

Rajwade et al. (2022) showed that Swift J1818.0–1607 exhibits an interesting fluctuating spin-down rate (see Fig. 1) and suggested that

* E-mail: rebecca.fisher-7@postgrad.manchester.ac.uk (RF)

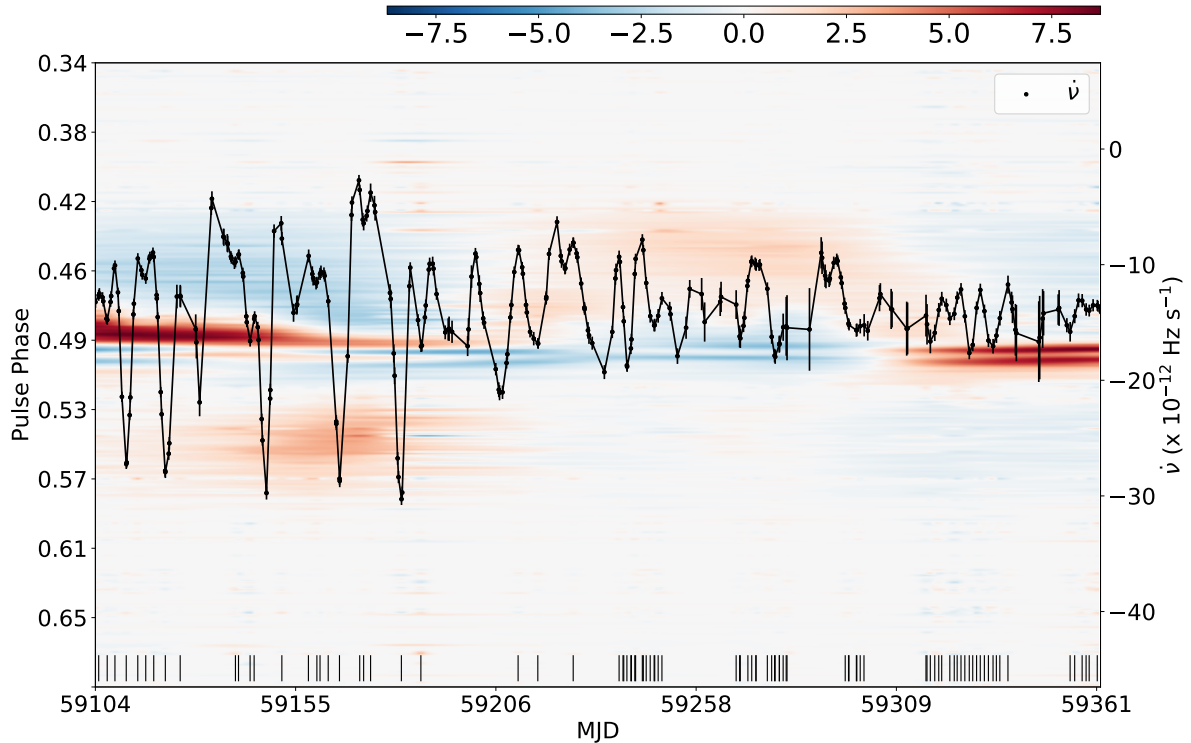


Figure 1. Gaussian Process variability map for the total intensity of the pulse profile over time. The spin-down variation has been overlaid to show that changes in the spin-frequency derivative, $\dot{\nu}$, modulation amplitude at MJDs 59185 and 59300 coincide with profile shape changes. The black vertical lines at the bottom of the plot indicate the dates of the observations. The colourbar units are the median of the standard deviation of all the off-pulse regions from the data set, with red indicating an excess in power compared to the median profile and blue a power deficit.

the magnitude of modulation of the spin-frequency derivative, $\dot{\nu}$ (related to the spin period, P , and its time derivative, \dot{P} , as $\dot{\nu} = -\dot{P}/P^2$), around the mean value may be correlated with profile shape. This suggests the magnetic braking torque may be linked to magnetospheric changes. Regular observations of the radio emission of Swift J1818.0–1607 carried out between September 2020 and May 2021 (MJDs 59104–59365) provide the opportunity to study the evolution of the pulse profile characteristics, such as polarisation and shape, and investigate any correlations with the spin-down behaviour, which may provide insight into the underlying physical causes. The paper is organised as follows: We describe the radio observations of the magnetar in section 2. Section 3 describes the radio pulse profile calibration method and section 4 describes the methods and results of the analysis used to investigate the evolution of these profiles. The findings are discussed in section 5 and summarised in section 6.

2 OBSERVATIONS

The observations were made using the 76-m Lovell Telescope and the 38×25 -m Mark II Telescope at the Jodrell Bank Observatory in the UK between MJDs 59104 and 59365 (see Table A1 for a full list of the observations used). The central frequency of the observations was 1.53 GHz with a bandwidth of 384 MHz, which was divided into 1532 channels. Each telescope has two orthogonal dipole receivers in combination with a quarter-wave plate, which converts the signal from linear to circular polarisation. The voltages are processed using the Digital Filter Backend (DFB) (Manchester et al.

2013), which converts the incoming data into frequency channels and generates Stokes parameters, enabling the linear and circular polarisations to be sampled. These data are folded onto 1024 phase bins using the best-known ephemeris for the magnetar, and the data were dedispersed using a dispersion measure (DM) of 699 pc cm^{-3} . These data were then summed into 8-second sub-integrations, resulting in time-frequency-Stokes parameters data cubes that are saved to disk. The majority of the data analysis was performed using the PSRCHIVE (Hotan et al. 2004) and PSRSALSA (Weltevrede 2016) packages. Channels affected by radio frequency interference (RFI) were removed using PSRCHIVE’s paz.

3 DATA ANALYSIS

3.1 Radio Pulse Profile Polarisation Calibration

The measured polarisation profiles were calibrated to account for how the telescope’s instrumentation responds to the incident radio waves. Polarisation errors can arise from the gains of the orthogonal dipole receivers being unequal (differential gain), the two feeds not being perfectly orthogonal causing mixing of the orthogonal polarisation components (leakage), imperfections or frequency dependence of the quarter-wave plate, and phase differences due to, for example, different cable lengths for the signals from each feed (differential phase). Some of these properties of the telescope can vary over the timescale of days. Calibration observations using a noise diode and well-known sources are used to calibrate pulsar profiles (e.g. van Straten 2004, 2013). However, at Jodrell Bank, the calibration observations are too

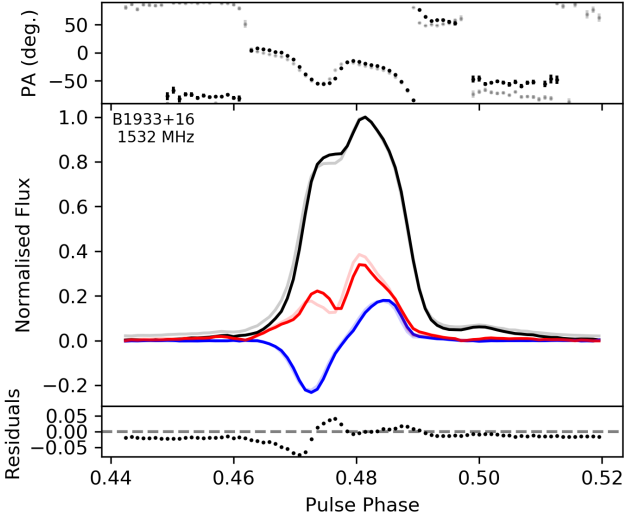


Figure 2. An example of a MTM-calibrated pulse profile from PSR B1933+16 showing the total intensity (black), linear polarisation (red) and circular polarisation (blue) as a function of pulse phase. The high S/N template (Johnston & Kerr 2018) is plotted behind in more transparent colours. The residuals from subtracting the total intensity of the template from the calibrated profile are shown in the bottom panel. The calibrated profile shape and PA are sufficiently well matched to the template that any variations in polarisation in the magnetar can be reliably identified.

infrequent, and so the method of Matrix Template Matching (MTM) (van Straten 2006) was used instead. This was performed using the PSRSALSA package (Weltevrede 2016).

In MTM, a pulsar with a high percentage of linear polarisation that exhibits stable polarisation properties is observed with the same telescope as the magnetar of interest, and its profile at that time is matched to its high signal-to-noise (S/N) template for a similar frequency, with a separate solution being produced for each frequency channel. In this case, the bright radio pulsar B1933+16 (Mitra et al. 2016) was used as it is observed regularly with the Lovell telescope in the same frequency band. Thus, its frequency-dependent profile could be matched to a high S/N calibrated template (Johnston & Kerr 2018) using PSRSALSA’s MTM routine `pca1` to obtain calibration solutions over time and frequency. Linear transformations of the Stokes parameters by Jones matrices are described by Mueller matrices, which have seven independent components (van Straten 2004). The solutions are determined by fitting a Mueller matrix operating on the Stokes parameters of the observed polarisation and are parameterised in terms of the system’s absolute gain, differential phase, and differential gain (Hamaker et al. 1996). The MTM process uses a non-linear least-squares fitting regime to find the parameters that best match the profile to its template. The resultant Mueller matrix solutions can then be applied to other profiles observed at a similar time and at a similar frequency.

The solutions were reapplied to the dispersion and Faraday rotation corrected B1933+16 pulsar profiles, and the data were dedispersed to produce calibrated profiles with the linear and circular polarisation components, as shown in Fig. 2. The profile shape and PA of the calibrated profiles were visually inspected with reference to the high S/N template to check that they were sufficiently well matched to the template such that any variations in polarisation in the magnetar can be reliably identified.

The solutions for the calibrator profile closest in date, with an

upper limit of half a day before or after the observation time, were then applied to the Swift J1818.0–1607 data, initially uncorrected for RM. The `pca1` routine applies the solutions on a frequency channel-by-channel basis. Therefore, we added a step in the process to extract the channels with a zero weight for which there was no solution and masked these using PSRCHIVE’s `paz` before applying the calibration solutions to ensure only frequency channels available from the calibrator profile were used. PSRSALSA’s `rmsynth` was then used on the calibrated files to obtain the RM for each observation by maximising the degree of linear polarisation (Ilie et al. 2019).

We decided to first use PSRCHIVE’s `rmfit` to Faraday rotate the data for RMs of 0–3000 rad m^{-2} in steps of 300 rad m^{-2} and find the value at which the linear polarisation was maximised to get an initial estimate before performing a finer RM search using `rmsynth`. Using `rmsynth` also provides a more reliable error estimate on the RMs using the method of bootstrapping (Weltevrede et al. 2012), whereby white noise with the same root mean square as measured in the off-pulse region is added to each frequency channel and the fitting is performed again for many iterations. This is more reliable as it makes no assumptions about the signal and can account for non-Gaussian distributed errors (Ilie et al. 2019). The mean value of the RMs was $1435 \pm 7 \text{ rad m}^{-2}$.

The MTM solutions were then applied to the files, and the profiles were corrected using the relevant RM value. The profiles were dedispersed and a parallactic angle correction was applied. The shape and polarisation features of the profile on MJD 59109.9 were cross-checked with the profile in Lower et al. (2021) on the same day and were found to be in good agreement. The total intensity shapes observed are broadly consistent with those shown in Rajwade et al. (2022) and Champion et al. (2020), which both use data from Jodrell Bank but with a different calibration method.

4 RESULTS

4.1 Radio Pulse Profile Polarisation Evolution

The linear and circular polarisation fractions were calculated by extracting the profile data and summing the flux density¹ in the on-pulse bins for each of the total intensity, I , linear, L , and circular, $|V|$, polarisation flux densities. The modulus of the circular polarisation was used to avoid cancellation if the handedness changed. The errors on the fractions were estimated as the root mean square noise in the off-peak bins of the baseline subtracted profile. The flux density uncertainty, δF , for each phase bin was taken to be the root mean square of the flux in the off-pulse region of the baseline-subtracted profile given by

$$\delta F = \sqrt{\frac{1}{N_{\text{off}} - 1} \sum_{i=1}^{N_{\text{off}}} F_i^2}, \quad (1)$$

where F_i is the flux density in bin i and N_{off} is the number of off-pulse bins. Using standard error propagation, the uncertainties on the flux densities in the on-pulse region were calculated.

The evolution of the linear and circular polarisation fractions is shown in Fig. 3. These fractions vary significantly with time, but there was no obvious correlation with the spin-down behaviour of the magnetar. The main peak of the profile in most cases exhibits a very high fraction of linear polarisation, although there are some exceptions to this. High linear polarisation fractions in the main peak

¹ Flux densities are not calibrated in this work and are therefore arbitrary.

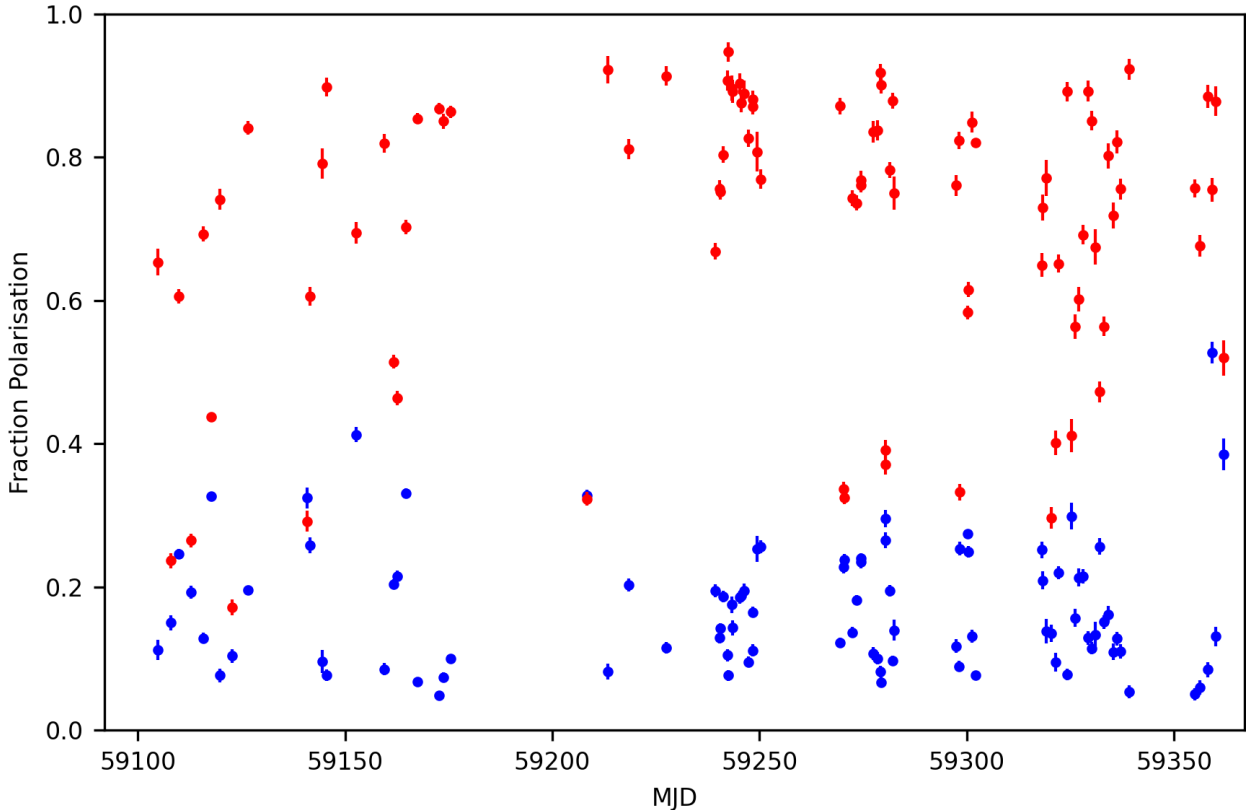


Figure 3. Evolution of the linear (red) and absolute circular (blue) polarisation fractions with MJD. The linear polarisation was generally high, and most profiles also exhibited significant circular polarisation.

are common in radio pulsars (Gould & Lyne 1998), although most pulsars do not show such variability in their polarisation properties over time. The high linear polarisation fractions are also consistent with both previous observations of this magnetar (Champion et al. 2020; Lower et al. 2020) and the other magnetars with radio emission (e.g. Kramer et al. 2007; Camilo et al. 2007a). The PA was found to vary considerably in shape, as shown by the example profiles in Fig. 4, and showed significant deviation from the rotating vector model S-like shape seen in many normal pulsars (Radhakrishnan & Cooke 1969). When the PA had a constant slope, as in the right-hand panel of Fig. 4, it had a range of gradients, including both positive and negative values. The PA of the main peak often demonstrated a drop like that shown in the middle panel of Fig. 4, but the magnitude of this drop also varied between observations. The PA was also seen to have wiggles similar to those seen in the magnetars XTE J1810–197 (Kramer et al. 2007; Dai et al. 2019) and PSR J1622–4950 (Levin et al. 2012) which could hint at propagation effects in the magnetosphere. Further analysis of the PA behaviour will be presented in future work (Liu et al. in prep).

The majority of the profiles also show significant circular polarisation, but the degree of circular polarisation is almost always lower than the linear polarisation fraction, as seen in many pulsars (Radhakrishnan & Rankin 1990). The handedness of the circular polarisation is generally the same across each profile, as seen in profiles of other pulsars with high degrees of linear polarisation (Han et al. 1998).

4.2 Gaussian Process Regression Analysis

Gaussian Process Regression (GPR) analysis was used to track the variability of the properties of the calibrated radio pulse profiles over time. The GPR software *PulsarPVC* (Shaw 2020) aligns the profiles based on their shape using cross-correlation. However, due to the high variation in the pulse profile shape and uncertainty as to whether features of the pulse profile stayed at the same pulse phase, we decided to modify this to align the profiles using the pulse arrival times to prevent potentially losing this shape information. This required generating a more precise timing model using the pulsar timing software *TEMPO2* (Hobbs et al. 2006), which we used to fit a model to the pulse TOAs based on the magnetar’s rotational frequency, ν , and its first six time derivatives. This gave a phase-connected timing solution for the magnetar over a span of 2 years. In order to do a comparative study of the pulse profile evolution, we decided to align the profiles, which meant whitening the TOAs. To do that, the differences between the actual and predicted TOAs were fitted with 125 sinusoidal waves using the *FITWAVES* method such that the residual of the fit was less than the time span of one pulse phase bin of the profile (spin period (1.36 s) divided by the number of phase bins (1024)) to ensure accuracy to within one bin. We note that the use of *FITWAVES* is for the sole purpose of roughly aligning the profiles to study the large-scale evolution, and we are insensitive to the daily pulse phase jitter in the profiles once the TOAs are whitened. The large number of waves needed is due to the magnetar’s high levels of timing noise. We note that this assumes that some fiducial point on the star is being tracked, and is possible

because of the high observing cadence of our data that allows us to reliably track the profile components. The pulse is almost always dominated by a single strong component, which, on short timescales, seems to be fairly stable in phase and has a width that varies between about 2-4% of the pulse period. Therefore, we adopted a simple, single-component template of width about 3% of the pulse period for the entire duration of these observations. The Mark II profiles were all flagged by PulsarPVC as being too low S/N to be included, and so they will not be considered further here. After alignment, each observed pulse profile was normalised by the mean on-pulse flux density and had the median of all the profiles subtracted from it to generate profile residuals.

A GPR model was generated for the evolution of the profile residuals over time for each phase bin across the pulse profile. A variability map was then produced, which shows how these differences vary over time with interpolation between observations. This was performed using PulsarPVC (Shaw 2020), which implements the method described in Brook et al. (2016). This uses the Matérn covariance kernel, which can model sharp changes in the profile residuals (Rasmussen & Williams 2005), combined with a white noise kernel, which allows the uncertainties, such as the white noise introduced by the telescope’s system temperature, in the profile data to be modelled. The GPR optimises the hyperparameters σ^2 , λ , and σ_n^2 using a maximum likelihood function. These hyperparameters describe the signal variance, the covariance lengthscale, and the noise variance of the data, respectively. The values of these parameters could provide insight into the underlying processes causing profile variability by characterising their temporal behaviour. We modified the lower limit of the search range for the hyperparameter λ from 30 days to 1 day to allow shorter timescale periodicities to be detected, something that is possible given the high cadence of our data set.

The resulting variability map for the pulse profiles’ total intensity is shown in Fig. 1. The colour scale indicates whether the profile has an excess (red) or deficit (blue) of power compared to the median profile. The colourbar scale is the median of the standard deviation of the off-pulse flux, and the range of values seen indicates the profile shows significant variability. The median value of λ for pulse phase 0.39-0.59 was 39.5 days, with a median absolute deviation of 9.5 days. Fig. 1 shows that the transitions in modulation amplitude of $\dot{\nu}$ at MJDs 59185 and 59300 (seen visually here but quantified by changes in a modulation index defined by Rajwade et al. (2022)) coincide with changes in the shape of the total-intensity radio profile. An example of a characteristic profile from each of these three modes is shown in Fig. 4. All plots have the same pulse phase ranges, with the profiles aligned according to the improved timing model. The profile evolves from having a trailing component that sometimes appears to exhibit an orthogonal-mode-like jump, then a leading component, and finally only exhibiting the main central component. From Fig. 1 it is also evident that there is still variability in the profile shape within the modes, although it is less significant than the variability between modes.

We also modified PulsarPVC to run on the linear polarisation component of the profiles. This produced the variability map shown in Fig. 5, and it is very similar to that for the total intensity shown in Fig. 1, but with the colours indicating a lower significance (ranging up to a maximum excess of approximately 6 standard deviations) and the transitions being less clear. This implies that the total and linear intensity components are closely related. The S/N of the circular polarisation component of the profiles was too low to produce a variability map.

4.3 Lomb-Scargle Periodogram Analysis

Fig. 6(a) shows the Lomb-Scargle periodogram² for $\dot{\nu}$ in blue for the whole period of profile data available (MJDs 59104-59365). The observed $\dot{\nu}$ signal is a product of the true underlying signal and a window function that describes the observation times. The window function was generated by creating an array with entries of unity for each date present and plotting it in yellow to allow peaks caused by aliasing or Nyquist-like limits to be identified. False alarm probabilities (FAPs) calculate the probability that a signal that does not have a periodic component will produce a peak of a given power. These are used to quantify peak significance. The most robust way to calculate FAPs is the bootstrap method because it does not make many assumptions about the distribution of the periodogram and accounts for window effects (VanderPlas 2018).

As shown in Fig. 6(a), three significant frequencies with peaks above the 0.3 FAP that do not coincide with any window function features were identified. The frequencies of these peaks were $0.059 \pm 0.002 \text{ days}^{-1}$, $0.084 \pm 0.003 \text{ days}^{-1}$, and $0.117 \pm 0.002 \text{ days}^{-1}$. These peaks look to be harmonically related based on their almost even frequency spacing and amplitude ratios. The fundamental frequency, however, appears to be missing.

The data were then split into the epochs for the three modes (MJDs 59104-59184, 59185-59299, 59300-59365) corresponding to when the amplitude of modulation in $\dot{\nu}$ and profile shape changes are seen in the GPR variability plot in Fig. 1. Lomb-Scargle analysis on $\dot{\nu}$ for each epoch is shown in Fig. 6. All three harmonics are present in the first mode; the second mode develops a new significant frequency at $0.100 \pm 0.003 \text{ days}^{-1}$; and in the third mode, harmonics two and four are present. This suggests that some of the harmonics persist throughout the data.

No significant periodicities or periodicities coinciding with the frequencies of the harmonics in $\dot{\nu}$ were found in other properties, such as the linear and circular polarisation fractions. This suggests that the profile variation on the shorter timescales within the modes is not directly correlated with the spin-down behaviour.

5 DISCUSSION

5.1 Radio Pulse Profile Polarisation Evolution

As shown in Fig. 3, the profiles generally have a high degree of linear polarisation and have a median value of $\sim 17\%$ circular polarisation across the profiles, both of which vary significantly over time, as is seen in other radio-loud magnetars (e.g. Camilo et al. 2007c; Levin et al. 2010; Shannon & Johnston 2013; Dai et al. 2019). This suggests the magnetosphere of the magnetar is very dynamic over a timescale of days. The main peak in most cases exhibits a very high amount of linear polarisation, although there are some exceptions to this. The trailing component that develops in the first mode almost always has a significant amount of linear polarisation. The PA associated with this part of the profile gradually develops a jump of about 60 degrees, which was also seen by Champion et al. (2020). This is an interesting feature, as, for an orthogonal polarisation mode, a jump of 90 degrees would be expected. Smaller jumps have been observed in other pulsars, and it has been suggested this could be due to the polarisation modes not being completely orthogonal (e.g. Smits et al. 2006). The profiles become depolarised between the two humps,

² This was implemented using the ASTROPY package for PYTHON with its default settings (Astropy Collaboration et al. 2013, 2018).

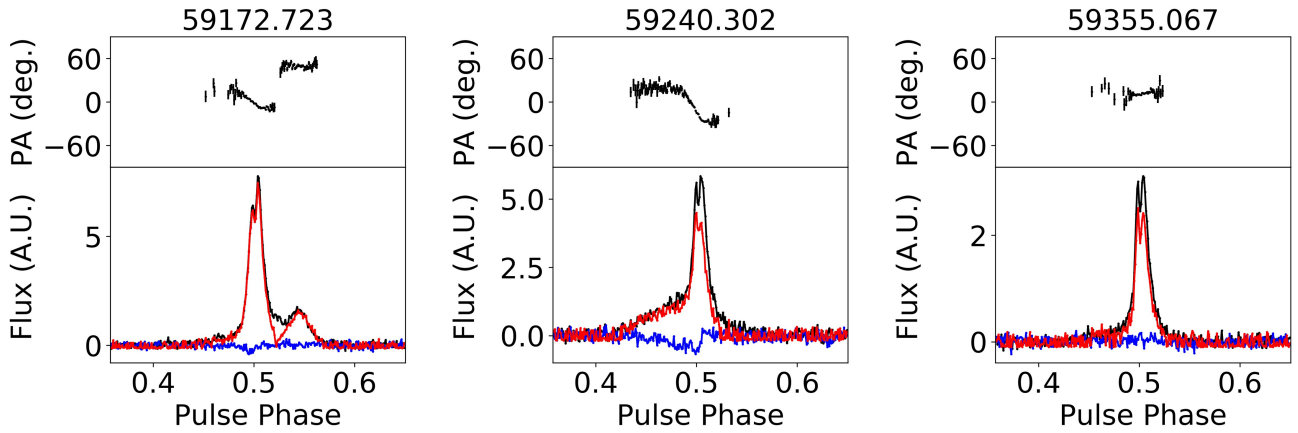


Figure 4. Example radio pulse profiles of Swift J1818.0–1607 that show the total intensity (black), linear polarisation (red), and circular polarisation (blue) flux density in arbitrary units of the pulse as a function of pulse phase. The linear polarisation position angles (PAs) are shown in the top panels. From left to right, the profiles shown are characteristic of the total intensity shapes seen in each of the three modes (MJDs 59104–59184, 59185–59299, 59300–59365) corresponding to the transitions in the amplitude of the spin-frequency derivative, $\dot{\nu}$, modulations, as can be seen in Fig. 1.

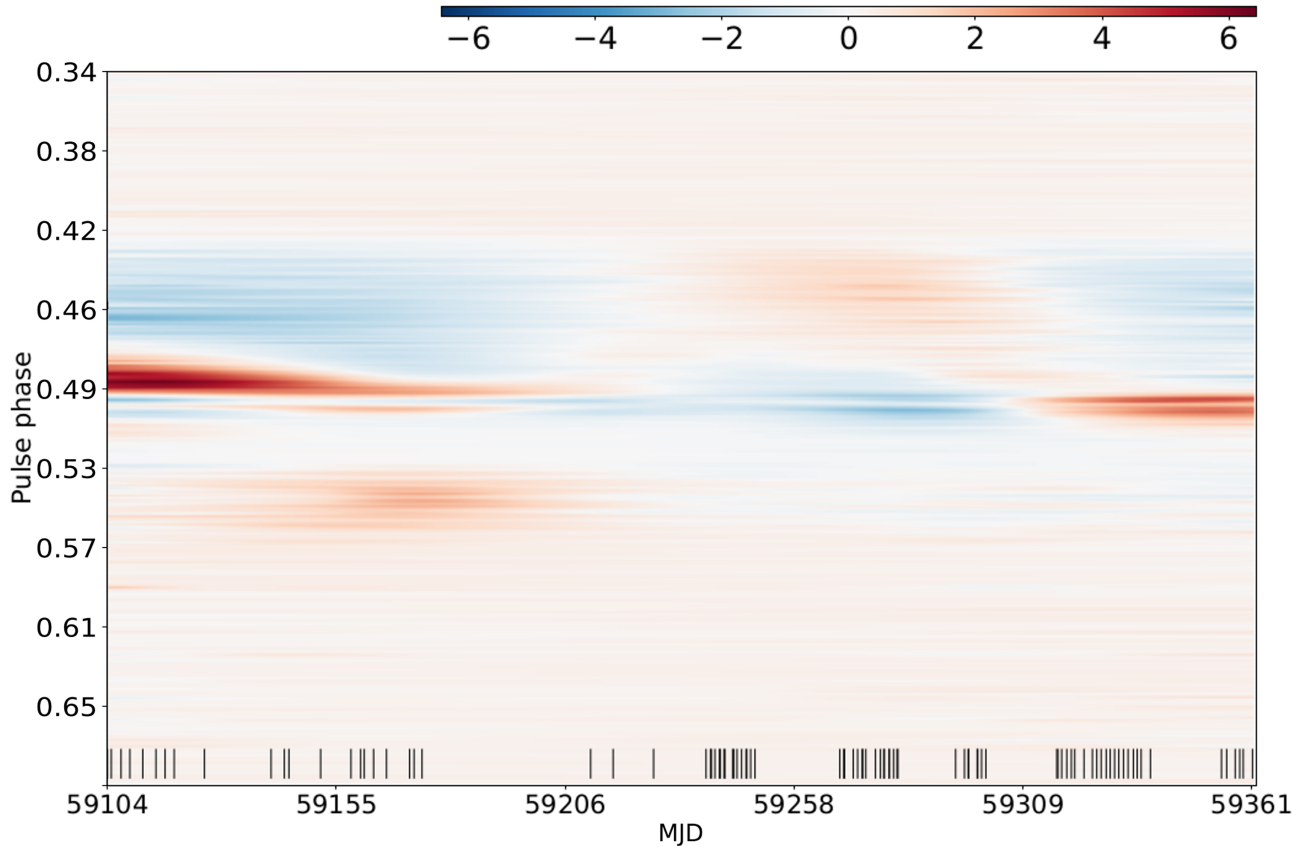


Figure 5. Gaussian Process variability map for the linear polarisation of the pulse profiles. The black vertical lines at the bottom of the plot indicate the dates of the observations. The colourbar units are the median of the standard deviation of all the off-pulse regions from the data set, with red indicating an excess in power compared to the median linear polarisation profile and blue a power deficit. The similarity between this plot and Fig. 1 demonstrates the high percentage of linear polarisation generally present in the pulse profiles followed the behaviour of the total intensity changes.

which is consistent with the mixing of modes (Lyne et al. 2022). A detailed analysis of the PA behaviour will be presented in future work (Liu et al. in prep). The circular polarisation varies across the pulse phase and could be due to either something intrinsic to the mechanism of radio emission or due to effects during propagation through

the magnetosphere (Petrova & Lyubarskii 2000). Partially coherent mixing between modes could produce both the observed wiggles seen in the PA and a significant amount of circular polarisation (e.g. Edwards & Stappers 2004; Oswald et al. 2023). A correlation between the variation in the linear and circular polarisations could be

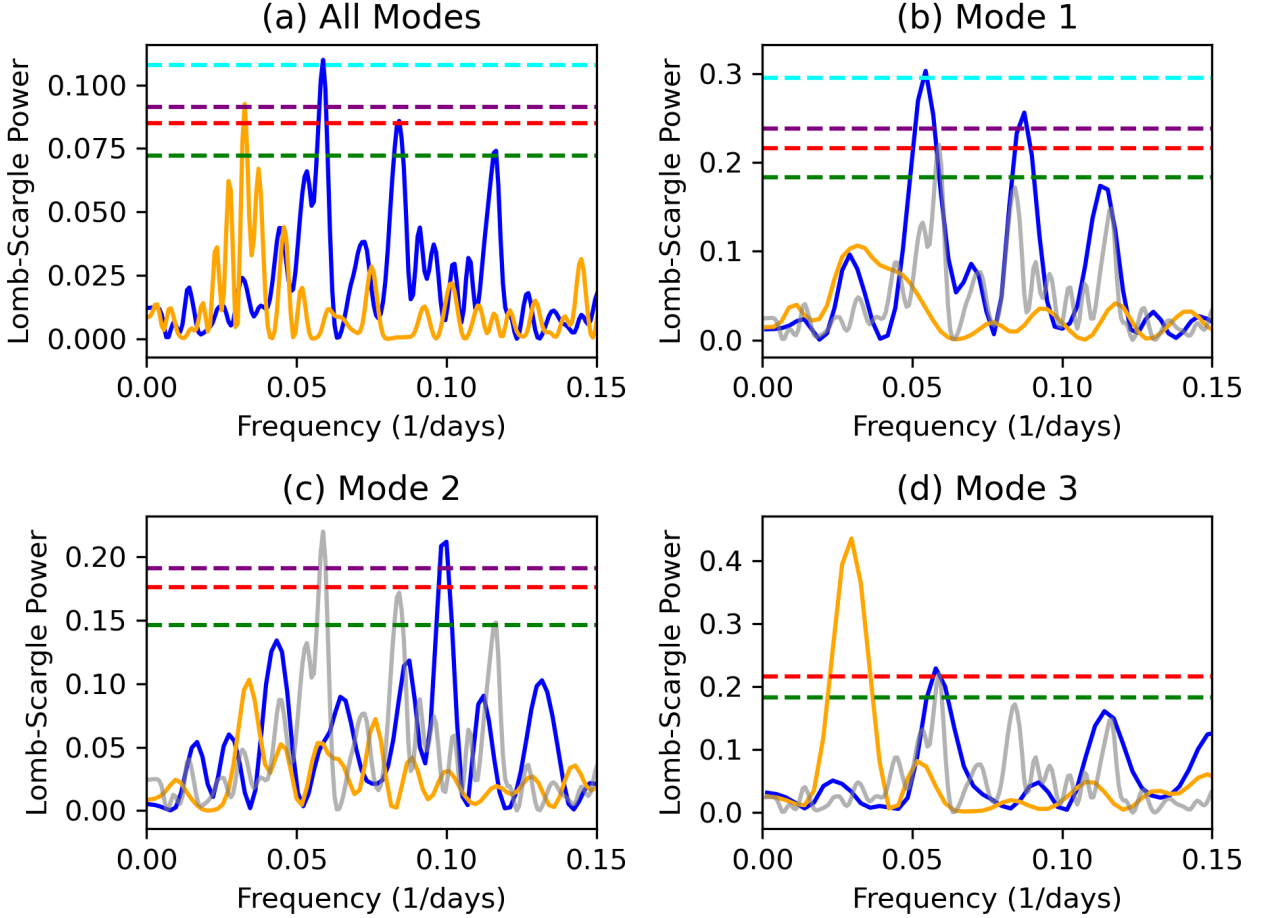


Figure 6. Lomb-Scargle periodograms for $\dot{\nu}$ are shown in blue for timescales covering all three modes and separately for each mode with their corresponding window functions in yellow. The 0.3, 0.1, 0.05, and 0.01 FAP levels are shown by the green, red, purple, and cyan dashed lines, respectively. The three peaks above the 0.3 FAP level in subplot (a) look to be harmonically related. The periodogram from subplot (a) scaled by a factor of two is shown in grey on the other subplots to show that all three peaks are present again in mode 1 (MJD 59104–59185), two are present in mode 3 (MJD 59300–59365), but in mode 2 (MJD 59185–59300), a new significant frequency emerges.

evidence of Faraday conversion (Edwards & Stappers 2004; Lower et al. 2023) due to propagation in the birefringent magnetosphere plasma surrounding the magnetar. Excluding profiles from the Mark II telescope and one outlier point with particularly high circular polarisation, the Pearson correlation coefficient between the circular polarisation fraction and one minus the linear polarisation fraction is 0.46 with p-value 3.4×10^{-6} . This suggests there is not a significant correlation, despite the fact that in some profiles, significant circular polarisation was observed to coincide with a reduction in linear polarisation compared to surrounding profiles. Further investigation of this possibility is left for future work. An investigation of this variability demonstrated no correlations between the changes in the polarisation fractions or PA features and other properties, such as the $\dot{\nu}$ variation, of the magnetar. There also appeared to be no significant periodicity to the variations in these fractions, and the variation could thus not be linked to the mechanism causing the spin-down variation.

5.2 Gaussian Process Regression Analysis

The variability plot produced by the GPR analysis in Fig. 1 for the evolution of the pulse profile shows the significant variability

of the profile shape. The high variability of the radio pulse profile shape and the levels of polarisation seen in individual profiles are consistent with those seen in the four other radio-loud magnetars: 1E 1547.0–5408 (Camilo et al. 2007c), PSR J1622–4950 (Levin et al. 2010), SGR J1745–2900 (Lee et al. 2013; Shannon & Johnston 2013) and XTE J1810–197 (e.g. Dai et al. 2019). The degree of variability over the timescale of days demonstrates the value of high-cadence data in observing magnetars. If observations were taken less frequently, the level of structure on these short timescales may be undetectable, and, similarly, this also implies that shorter-term variability and patterns may also be missed.

The evolution through the three modes corresponding to the characteristic profile shapes shown in Fig. 4 can be seen clearly in Fig. 1. The overlaid spin-frequency derivative data show that the major changes in profile shape coincide with changes in the amplitude of modulation of the $\dot{\nu}$ variation at MJDs of approximately 59185 and 59300, providing more conclusive evidence for this suggestion than when it was first postulated by Rajwade et al. (2022). The variability maps in Fig. 1 and Fig. 5 show that the transitions between modes occur suddenly compared to the duration of the modes.

The mode changes seen in this magnetar are comparable to the

phenomenon of mode changing seen in some pulsars. These pulsars can similarly display periods of quasi-stable emission between sharp discontinuous changes (e.g. [Backer 1970](#); [Wang et al. 2007](#)). These changes are very rapid, usually occurring over a single period, and can affect the shape and polarisation of the pulse profile. This dramatic variation is potentially attributable to large-scale redistribution of currents within a pulsar’s magnetosphere, inducing a change to the radio-emission beam pattern and hence a change to the pulse profile (e.g. [Wang et al. 2007](#)). As discussed by [Wang et al. \(2007\)](#), this suggestion accounts for both the different mode lengths and the short transition timescale: if one of many random perturbations happens to induce positive feedback whereby a small change in magnetospheric currents leads to a change in the electric field, which further enhances this current, rapid large-scale redistribution of currents can result. [Kramer et al. \(2007\)](#) found evidence for how changes in plasma density within a magnetosphere at the point of radio emission production may affect the spin-down rate and could lead to changes in the pulse profile. Emission mode switching has been observed previously in Swift J1818–1607 by [Lower et al. \(2021\)](#) and [Champion et al. \(2020\)](#). These authors note that discrete switching between profile shape modes has been seen to modify the pulse profiles of other magnetars, including affecting the leading edge and causing the development of a secondary trailing component. Mode switching has also been found to cause a trailing component in the profile of the high-B pulsar PSR J1119–6127 ([Weltevrede et al. 2011](#)), which bears resemblance to the changes in the profiles observed here.

The correlation between the modulation amplitude of $\dot{\nu}$ and the profile shape changes suggests a link between the spin and the radio emission from the magnetar. This has been observed in normal pulsars by [Lyne et al. \(2010\)](#), [Brook et al. \(2016\)](#), and [Shaw et al. \(2022\)](#), who attributed this to changing plasma densities in the polar cap region. Changes to plasma density in a magnetosphere, as well as currents within it, can change the torque acting on a pulsar, which affects the spin-down rate ([Kramer et al. 2006](#); [Li et al. 2012](#)). Interestingly, unlike the observations by [Shaw et al. \(2022\)](#), we see changes to the size of fluctuations of $\dot{\nu}$ around a constant value rather than changes to the absolute value of $\dot{\nu}$. This is perhaps a hint that there are changes to the magnetosphere on different scales, with smaller changes affecting the spin-down but not having a significant effect on the pulse profile. This may be the case if there are current changes in the magnetosphere close to the light cylinder, which can have a large effect on the torque acting on a magnetar without global magnetospheric changes, which would affect the radio emission ([Stairs et al. 2019](#)). The changes to the magnetospheric plasma could also be linked to a strong twist that has developed in the magnetosphere and an associated stronger spin-down torque caused by a stronger magnetic field at the light cylinder ([Thompson et al. 2002](#)). The field could subsequently untwist due to crustal movement. This would result in a decreasing torque and hence reduced amplitude of $\dot{\nu}$ and its fluctuations, which are reminiscent of damped oscillations, as seen in this magnetar and others such as XTE J1810–197 ([Camilo et al. 2016](#); [Levin et al. 2019](#)). The timescales of $\dot{\nu}$ oscillations for normal pulsars are longer than those seen here, which is consistent with magnetars having more dynamic magnetospheres, stronger and more variable currents, and higher rates of pair creation.

Although the correlation between the spin-down and pulse shape changes points to a magnetospheric cause, an alternative explanation is precession. This would cause the angle between the magnetic dipole and rotation axes of the star to vary periodically and cause the spin-down rate to vary. The pulse profile would also change as a result of a changing line of sight across the beam. In normal pulsars, the expected period of precession is much longer than the changes

seen here, and it is expected to be strongly damped by the pinning of superfluid vortices inside the star ([Link 2006](#)), so the magnetospheric explanation is usually preferred ([Lyne et al. 2010](#)). However, it has been suggested that the strong magnetic fields of magnetars could not only deform the star and excite large-amplitude precession but also shatter the crust or suppress the neutron superfluidity, allowing precession to occur ([Wasserman et al. 2022](#)). Since we do not see profile changes corresponding to each oscillation of $\dot{\nu}$, precession seems less able to account for our observations here, and so, a magnetospheric cause seems more likely, but still does not fully explain the lack of profile changes associated with the oscillations.

5.3 Lomb-Scargle Periodogram Analysis

The existence of discrete frequencies in $\dot{\nu}$ on timescales shorter than the major mode changes shown in Fig. 6(a) that appear to be harmonically related could point to free oscillations caused by seismic activity. It has been proposed that the outbursts of magnetars could excite toroidal oscillations of the star, which propagate into the magnetosphere, increasing the voltage in the polar cap region and making radio emission more likely ([Morozova et al. 2012](#)). It is also expected that the oscillations will increase the size of the polar cap and radio emission beam ([Lin et al. 2015](#)). The damping of the oscillations means the size of the effect will decay with time. The decreasing profile width shown in Fig. 4 would be consistent with a shrinking polar cap as the toroidal oscillations decay.

The subplots shown in Fig. 6(b) and (d) show that harmonics two and four persist, perhaps suggesting a common cause or mechanism that persists across the modes. Fig. 6(c) shows the emergence of a new significant periodicity. This could be explained by a change in the dominance of the seismic oscillation modes, which causes magnetospheric changes and thus coincides with the mode changes in the profile shape. This could be consistent with the suggestion that when the oscillations of seismic modes exceed a critical value, they could cause mode changes in pulsars ([Lin et al. 2015](#)). The lack of the fundamental mode frequency is puzzling, as in stellar oscillations, the lower overtone modes are expected to be the most strongly excited. At present, there are no theoretical predictions as to whether seismic oscillations with frequencies of days could be produced based on predictions of the structure of magnetars.

Although we conclude above that precession is an unlikely explanation for our observations, we note that it could provide an alternative explanation for the persisting periodicity since it would cause strong coupling between magnetospheric variations and the spin-down torque. The precession period is of order P/ϵ , where P is the magnetar’s spin period and ϵ is the star’s ellipticity ([Wasserman et al. 2022](#)). Upper limits for ϵ considering the elasticity of the crust and magnetic deformation ([Desvignes et al. 2022](#)) result in a prediction for the precession period of around 16 days and 252 days, respectively. The elastic crust strain ϵ could give a precession period on the correct timescale for the periodicities seen. Precession has been invoked to explain 16-day periodicities in a fast radio burst, which are thought to be related to magnetars ([Tong et al. 2020](#)).

Quasi-periodic variations in $\dot{\nu}$ are seen in other magnetars such as 1E 1048.0–5937 ([Archibald et al. 2015](#)) and also in some rotation-powered radio pulsars ([Kramer et al. 2006](#); [Lyne et al. 2010](#); [Shaw et al. 2022](#)) on longer timescales. The spin-down torque in untwisting magnetar magnetospheres is expected to vary in a non-monotonic way ([Beloborodov 2009](#)), which could account for the fluctuating behaviour of $\dot{\nu}$. However, it has been argued by [Tong et al. \(2013\)](#) that short-term spin-down variations in magnetar PSR J1622–4950, on similar timescales to those seen here in Swift J1818.0–1607, are

hard to explain using the theory of magnetospheric untwisting (Beloborodov 2009) and could instead be explained by a particle wind. In the particle wind braking model, it is predicted that the spin-down would exhibit behaviour in the higher-order derivatives (Tong et al. 2013) due to the torque from the distortion of the dipole field near the light cylinder affecting the spin-down of the magnetar (Harding et al. 1999). This explanation could also link to seismic aftershocks, which can produce variations in the particle wind (Thompson & Duncan 1996), allowing it to vary significantly on shorter timescales and cause timing noise. This mechanism has been suggested to explain the timing noise of normal pulsars, in which case the wind is rotation-powered (Lyne et al. 2010), but it could be powered by the decay of the magnetic field of the magnetar (Tong et al. 2013). This mechanism of wind braking is thought to not change the global dipole field of the magnetar (Tong et al. 2013), and this could explain why the overall profile shape stays reasonably stable within each mode. The modes themselves could instead be a result of a global magnetospheric reconfiguration (Shaw et al. 2022). Further supporting evidence for the wind braking model would be the presence of a pulsar wind nebula powered by the magnetar. Extended diffuse emission has been detected in X-ray and radio for Swift J1818.0–1607 (Ibrahim et al. 2023), but there is no strong evidence for this being a nebula, and it may be a dust scattering halo.

While the magnitude of the oscillations in $\dot{\nu}$ is clearly correlated with the pulse profile mode changes, the lack of coinciding periodicities in any of the Lomb-Scargle periodogram analyses on all other profile parameters suggests variability within the profile modes is not strongly coupled to the $\dot{\nu}$ oscillations or the underlying mechanism. In the study of the pulse profile variability of normal pulsars in Shaw et al. (2022), it was suggested that more subtle changes in the profile caused by smaller magnetospheric changes would not be able to affect $\dot{\nu}$ in an observable way. While the pulse variability within each profile mode did not exhibit periodic behaviour, the variability plot in Fig. 1 does seem to show there was a greater degree of variability earlier on. For example, in mode 1, there is the appearance of the trailing profile component, and there is variability in the leading slope in mode 2, compared to a much more consistent narrow peak in mode 3. This could imply that the greater the width or complexity of the profile, and hence the radio-emitting region, the greater the magnitude and complexity of the effects on the spin-down torque. Complex interactions, delays, or feedback could mean that there is no simple relationship between profile characteristics, and spin-down variations may be the cumulative effect of many processes.

6 SUMMARY

The radio emission properties of the magnetar Swift J1818.0–1607 seem to be in agreement with many of the suggested explanations for magnetar emission. However, it also demonstrates complex, highly variable behaviour that is not fully understood. The onset of radio emission after an X-ray outburst and the characteristics such as the decaying flux and wide beam are in agreement with emission from the j-bundle in a magnetosphere that is twisted by seismic activity in the neutron star crust and subsequently untwists (Beloborodov 2009). The clear correlation between the major profile shape mode changes and the amplitude of the spin-frequency derivative variations shown in Fig. 1 is in strong support of a twisted magnetic field exerting a torque on the magnetar (Thompson et al. 2002). The narrowing profile is consistent with a shrinking emission region and suggests these profile shapes reflect emission from different regions of the beam. The presence of harmonically related frequencies from the

Lomb-Scargle analysis of $\dot{\nu}$ shown in Fig. 6 could potentially point to seismic oscillation modes (Morozova et al. 2012; Lin et al. 2015) and may also link to a particle wind that could cause both timing noise and the emission to vary (Tong et al. 2013). The high variability in the pulse profile shape within the modes and $\dot{\nu}$ points to a dynamic magnetosphere. The lack of correlation between the $\dot{\nu}$ variation and profile features within the modes could be explained either by the fact that the variability in the magnetosphere can't produce observable changes (Shaw et al. 2022) or that the processes are too complex to produce simple correlations.

ACKNOWLEDGEMENTS

Access to the Lovell telescope and the Mark II telescope is supported by a consolidated grant from the UK Science and Technology Facilities Council (STFC). K.M.R. acknowledges support from the Vici research program 'ARGO' with project number 639.043.815, financed by the Dutch Research Council (NWO). The authors would like to thank the anonymous referee, whose comments significantly improved the manuscript.

DATA AVAILABILITY

The data used in this manuscript will be made available to others upon reasonable request to the authors.

REFERENCES

- Archibald R. F., Kaspi V. M., Ng C. Y., Scholz P., Beardmore A. P., Gehrels N., Kennea J. A., 2015, *ApJ*, **800**, 33
- Astropy Collaboration et al., 2013, *A&A*, **558**, A33
- Astropy Collaboration et al., 2018, *AJ*, **156**, 123
- Backer D. C., 1970, *Nature*, **228**, 42
- Beloborodov A. M., 2009, *ApJ*, **703**, 1044
- Brook P. R., Karastergiou A., Johnston S., Kerr M., Shannon R. M., Roberts S. J., 2016, *MNRAS*, **456**, 1374
- Camilo F., Reynolds J., Johnston S., Halpern J. P., Ransom S. M., van Straten W., 2007a, *ApJ*, **659**, L37
- Camilo F., et al., 2007b, *ApJ*, **663**, 497
- Camilo F., Ransom S. M., Halpern J. P., Reynolds J., 2007c, *ApJ*, **666**, L93
- Camilo F., Reynolds J., Johnston S., Halpern J. P., Ransom S. M., 2008, *ApJ*, **679**, 681
- Camilo F., et al., 2016, *ApJ*, **820**, 110
- Champion D., et al., 2020, *MNRAS*, **498**, 6044
- Dai S., et al., 2018, *MNRAS*, **480**, 3584
- Dai S., et al., 2019, *ApJ*, **874**, L14
- Desvignes G., et al., 2022, preprint (doi:10.21203/rs.3.rs-2281053/v1)
- Edwards R. T., Stappers B. W., 2004, *A&A*, **421**, 681
- Gould D. M., Lyne A. G., 1998, *MNRAS*, **301**, 235
- Hamaker J. P., Bregman J. D., Sault R. J., 1996, *A&AS*, **117**, 137
- Han J. L., Manchester R. N., Xu R. X., Qiao G. J., 1998, *MNRAS*, **300**, 373
- Harding A. K., Contopoulos I., Kazanas D., 1999, *ApJ*, **525**, L125
- Hobbs G. B., Edwards R. T., Manchester R. N., 2006, *MNRAS*, **369**, 655
- Hotan A. W., van Straten W., Manchester R. N., 2004, *Publ. Astron. Soc. Australia*, **21**, 302
- Hu C.-P., et al., 2020a, *ApJ*, **902**, 1
- Hu C.-P., et al., 2020b, *The Astronomer's Telegram*, **13588**, 1
- Ibrahim A. Y., et al., 2023, *ApJ*, **943**, 20
- Ilie C. D., Johnston S., Weltevrede P., 2019, *MNRAS*, **483**, 2778
- Johnston S., Kerr M., 2018, *MNRAS*, **474**, 4629
- Karuppusamy R., et al., 2020, *The Astronomer's Telegram*, **13553**, 1
- Kaspi V. M., Beloborodov A. M., 2017, *ARA&A*, **55**, 261
- Keith M. J., Johnston S., Levin L., Bailes M., 2011, *MNRAS*, **416**, 346

- Kirsten F., Snelders M. P., Jenkins M., Nimmo K., van den Eijnden J., Hessels J. W. T., Gawroński M. P., Yang J., 2021, *Nature Astronomy*, **5**, 414
- Kramer M., Lyne A. G., O'Brien J. T., Jordan C. A., Lorimer D. R., 2006, *Science*, **312**, 549
- Kramer M., Stappers B. W., Jessner A., Lyne A. G., Jordan C. A., 2007, *MNRAS*, **377**, 107
- Lee K. J., et al., 2013, *ATel*, **5064**, 1
- Levin L., et al., 2010, *ApJ*, **721**, L33
- Levin L., et al., 2012, *MNRAS*, **422**, 2489
- Levin L., et al., 2019, *MNRAS*, **488**, 5251
- Li J., Spitkovsky A., Tchekhovskoy A., 2012, *ApJ*, **746**, L24
- Lin M.-X., Xu R.-X., Zhang B., 2015, *ApJ*, **799**, 152
- Link B., 2006, *A&A*, **458**, 881
- Lower M. E., Shannon R. M., Johnston S., Bailes M., 2020, *ApJ*, **896**, L37
- Lower M. E., Johnston S., Shannon R. M., Bailes M., Camilo F., 2021, *MNRAS*, **502**, 127
- Lower M. E., et al., 2023, *arXiv e-prints*, p. arXiv:2311.04195
- Lyne A., Hobbs G., Kramer M., Stairs I., Stappers B., 2010, *Science*, **329**, 408
- Lyne A. G., Graham-Smith F., Stappers B., 2022, *Pulsar astronomy*, 5 edn. Cambridge University Press, Cambridge, UK
- Manchester R. N., et al., 2013, *Publ. Astron. Soc. Australia*, **30**, e017
- Mitra D., Rankin J., Arjunwadkar M., 2016, *MNRAS*, **460**, 3063
- Morozova V. S., Ahmedov B. J., Zanotti O., 2012, *MNRAS*, **419**, 2147
- Oswald L. S., Karastergiou A., Johnston S., 2023, *MNRAS*, **525**, 840
- Petrova S. A., Lyubarskii Y. E., 2000, *A&A*, **355**, 1168
- Radhakrishnan V., Cooke D. J., 1969, *Astrophys. Lett.*, **3**, 225
- Radhakrishnan V., Rankin J. M., 1990, *ApJ*, **352**, 258
- Rajwade K., et al., 2020, *The Astronomer's Telegram*, **13554**, 1
- Rajwade K. M., et al., 2022, *MNRAS*, **512**, 1687
- Rasmussen C. E., Williams C. K. I., 2005, *Gaussian Processes for Machine Learning*. Adaptive Computation and Machine Learning series, MIT Press, Cambridge
- Shannon R. M., Johnston S., 2013, *MNRAS*, **435**, L29
- Shaw B., 2020, *PulsarPVC*, <https://gitlab.com/benjaminshaw/pulsarpvc>
- Shaw B., et al., 2022, *MNRAS*, **513**, 5861
- Smits J. M., Stappers B. W., Edwards R. T., Kuijpers J., Ramachandran R., 2006, *A&A*, **448**, 1139
- Stairs I. H., et al., 2019, *MNRAS*, **485**, 3230
- Stamatikos M., et al., 2020, *GRB Coordinates Network*, **27384**, 1
- Thompson C., Duncan R. C., 1996, *ApJ*, **473**, 322
- Thompson C., Lyutikov M., Kulkarni S. R., 2002, *ApJ*, **574**, 332
- Tong H., Xu R. X., Song L. M., Qiao G. J., 2013, *ApJ*, **768**, 144
- Tong H., Wang W., Wang H.-G., 2020, *Research in Astronomy and Astrophysics*, **20**, 142
- VanderPlas J. T., 2018, *ApJS*, **236**, 16
- Wang N., Manchester R. N., Johnston S., 2007, *MNRAS*, **377**, 1383
- Wasserman I., Cordes J. M., Chatterjee S., Batra G., 2022, *ApJ*, **928**, 53
- Weltevrede P., 2016, *A&A*, **590**, A109
- Weltevrede P., Johnston S., Espinoza C. M., 2011, *MNRAS*, **411**, 1917
- Weltevrede P., Wright G., Johnston S., 2012, *MNRAS*, **424**, 843
- van Straten W., 2004, *ApJS*, **152**, 129
- van Straten W., 2006, *ApJ*, **642**, 1004
- van Straten W., 2013, *ApJS*, **204**, 13

APPENDIX A: OBSERVATIONS

This paper has been typeset from a $\text{\TeX}/\text{\LaTeX}$ file prepared by the author.

Table A1. Table of observations used with their telescope, start time, duration, and MJDs. All observations had a central frequency of 1.53 GHz and a bandwidth of 384 MHz.

Telescope	Time Start (hhmmss)	Duration (s)	Topocentric MJDs	Telescope	Time Start (hhmmss)	Duration (s)	Topocentric MJDs
Lovell	172854	1238.8	59105.729	Mark II	045009	3468.5	59275.202
Lovell	215627	1388.9	59107.914	Mark II	100843	3329.3	59275.423
Lovell	212904	728.5	59109.895	Lovell	082200	399.8	59277.349
Lovell	190442	538.9	59112.795	Lovell	110739	708.2	59278.464
Lovell	181407	888.2	59115.76	Lovell	050211	709.5	59279.21
Lovell	191633	798.1	59117.803	Lovell	083701	719.1	59279.359
Lovell	203052	719.0	59119.855	Lovell	100059	709.5	59280.418
Lovell	195441	709.4	59122.83	Lovell	110246	719.1	59280.46
Lovell	153315	1828.2	59126.648	Lovell	095129	708.2	59281.411
Lovell	194549	708.1	59140.824	Lovell	043035	698.6	59282.188
Lovell	144259	708.1	59141.613	Lovell	093405	148.7	59282.399
Lovell	140400	708.1	59144.586	Mark II	034717	3233.9	59291.158
Lovell	145522	698.6	59145.622	Mark II	090549	3498.6	59291.379
Lovell	174555	719.1	59152.74	Mark II	034319	3468.6	59292.155
Lovell	132013	908.7	59159.556	Mark II	090148	3508.1	59292.377
Lovell	173250	719.1	59161.731	Mark II	043829	3197.0	59293.194
Lovell	125129	709.5	59162.536	Mark II	085746	839.2	59293.374
Lovell	151647	668.6	59164.637	Mark II	091558	1717.9	59294.386
Lovell	124941	1837.9	59167.535	Mark II	033136	1195.3	59295.147
Lovell	172028	708.2	59172.723	Mark II	084959	3508.2	59295.368
Lovell	173026	719.1	59173.73	Mark II	040653	3609.1	59296.172
Lovell	122059	708.2	59175.515	Mark II	094554	3449.5	59296.407
Lovell	100251	708.2	59208.419	Lovell	080700	296.1	59297.338
Lovell	090335	719.1	59213.378	Lovell	043322	708.2	59298.19
Lovell	103252	717.7	59218.44	Lovell	072543	551.3	59298.31
Lovell	123143	709.5	59227.522	Lovell	045017	719.1	59300.202
Lovell	071435	698.6	59239.302	Lovell	074959	708.2	59300.327
Lovell	071401	659.0	59240.302	Lovell	042849	278.4	59301.187
Lovell	115849	698.6	59240.499	Lovell	041139	3609.2	59302.175
Lovell	072117	728.6	59241.307	Mark II	024813	839.2	59306.117
Lovell	074802	717.7	59242.325	Mark II	080637	3528.7	59306.338
Lovell	111543	719.1	59242.469	Lovell	014405	709.6	59318.072
Lovell	074816	349.3	59243.325	Lovell	075539	708.2	59318.331
Lovell	125634	719.1	59243.539	Lovell	041947	237.4	59319.181
Lovell	062221	627.7	59245.266	Lovell	074621	708.2	59320.324
Lovell	123158	708.2	59245.522	Lovell	082259	698.7	59321.35
Lovell	060648	518.5	59246.255	Lovell	024033	1277.2	59322.112
Lovell	065138	709.5	59247.286	Lovell	043538	578.6	59324.192
Lovell	065823	709.5	59248.291	Lovell	075601	708.2	59325.331
Lovell	104636	717.7	59248.449	Lovell	015330	708.2	59326.079
Lovell	074945	148.7	59249.326	Lovell	012506	436.7	59327.059
Lovell	070637	566.3	59250.296	Lovell	010308	708.2	59328.044
Mark II	062034	1258.1	59252.264	Lovell	042253	717.8	59329.183
Mark II	113909	2297.8	59252.486	Lovell	014409	717.8	59330.073
Mark II	061245	1318.1	59254.259	Lovell	012657	719.1	59331.061
Mark II	112329	2139.5	59256.475	Lovell	001204	719.1	59332.009
Mark II	100054	2948.7	59257.417	Lovell	012607	698.7	59333.06
Mark II	112823	2258.2	59260.478	Lovell	021847	719.1	59334.097
Mark II	054508	3478.0	59261.24	Lovell	065152	719.1	59335.286
Lovell	081627	608.6	59269.345	Lovell	031848	687.8	59336.138
Lovell	053719	708.2	59270.235	Lovell	003926	719.1	59337.028
Lovell	094920	708.2	59270.41	Lovell	024258	709.6	59339.113
Mark II	050553	1379.5	59271.213	Lovell	013630	708.3	59355.067
Mark II	102433	3498.5	59271.434	Lovell	054600	698.7	59356.241
Mark II	050156	1667.4	59272.21	Lovell	034107	717.8	59358.154
Lovell	083934	708.2	59272.361	Lovell	040406	719.2	59359.17
Mark II	045802	3388.0	59273.207	Lovell	230258	709.6	59359.961
Lovell	082102	709.5	59273.348	Lovell	005248	708.3	59362.037
Mark II	045406	3468.5	59274.204				
Lovell	092504	717.7	59274.393				
Lovell	111803	709.5	59274.471				